

Dear Dr. Florian Fuisseis,

We are delighted to submit the revised version of our manuscript, entitled 'Micro- and nanoporosity of the active Alpine Fault zone, New Zealand' for consideration for publication in Solid Earth.

Herein, we investigated and analyzed the state of porosity within rocks from the fault core of a major active fault – the Alpine Fault of New Zealand. By the means of synchrotron X-ray microtomography and transmission electron microscopy, we acquired unique data obtained from samples recovered during the first phase of the Deep Fault Drilling Project (DFDP-1B). Our results demonstrate extremely low total porosities in these rocks, which we suggest were reduced due to post seismic recovery mechanisms. We conclude that these low porosities in the presence of fluids possibly control the mechanical behavior of the fault and could trigger a seismic slip along the fault due to fluid pressurization and/or precipitation of weak mineral phases.

We have revised the manuscript taking into account reviewers' comments. We have copied the reviews below and addressed each comment in turn. Our responses are indicated in green text. We used track changes to document the revisions to the manuscript and are resubmitting both a track changes, and changes accepted versions. We refer to revisions in the manuscript by line numbers – these are correct with respect to the revised version with changes accepted.

The affiliations of the corresponding author (Martina Kirilova) and Klaus Gessner have changed during the review process, thus those are now updated in the revised manuscript.

Thank you for your consideration of this manuscript.

Regards,  
Martina Kirilova  
Corresponding Author  
[martina.kirilova@uni-mainz.de](mailto:martina.kirilova@uni-mainz.de)  
On behalf of the authors: Virginia Toy, Katrina Sauer,  
François Renard, Klaus Gessner, Richard Wirth, and  
Xianghui Xiao

# Interactive comment on “Micro- and nano-porosity of the active Alpine Fault zone, New Zealand” by Martina Kirilova et al.

James Gilgannon (Referee)

james.gilgannon@geo.unibe.ch

Received and published: 19 June

2020

Dear Editor,

As requested, I have reviewed the manuscript titled “Micro- and nano-porosity of the active Alpine Fault zone, New Zealand” by Kirilova et al., please find my general and specific comments below. Kirilova et al. present data from the analysis of a core recovered during the Deep Fault Drilling Project (DFDP-1B). Synchrotron X-ray microtomography (XCT) was used in conjunction with Transmission electron microscopy (TEM) to gain information about the porosity and its habit during the critical pre-rupture stage of a major fault’s seismic cycle. These results are used to discuss the potential differences in processes that are active in and around the Alpine fault and ultimately how this could effect a fault’s transition to the next stage of its seismic cycle.

General comments:

This being said I have a few suggestions for the authors to consider in my specific comments. The majority of which relate to the methods section, where I think that some of the explanation should be reformulated and details added, alongside a suggestion of a figure to help the reader. Additionally, I think there is a need to better link the XCT and TEM data sets to enrich the results and hence shore up the discussion. I have one less trivial concern that I would like the authors to address: stated here briefly, I am uncertain about how much can be made of a difference of 0.14% porosity between samples given the filtering methods used. The authors use this difference as part of the main discussion on how changes in porosity will affect a major fault’s mechanical state and I think that the significance of the result needs to be unpacked and evaluated more in the text. Lastly, I think the authors should be careful with when they say they ‘demonstrate’ or ‘show’ that certain processes are active. The results of this contribution are almost singularly observations about the characteristics of each sample’s porosity and in this sense the authors do not show but rather interpret the presence of fluids or the activity of pressure solution. I think this is an important distinction to be drawn.

Response: Thank you for this summary and the constructive comments. We have addressed each one of them following the specific comments below.

Specific comments:

I have tried to group the comments into blocks and they are ordered mostly in sequence with the order of the manuscript.

## 1. Comment on methods

As it stands I think the methods section needs bolstering in places. Below I have noted where I think the manuscript could benefit from this:

#### Lines 104 - 134: Analyses of XCT datasets

The structure here gives the feeling that you tired one method but subsequently chose another over it. After reading the manuscript over a few times I can see that this is not the case and you actually use both methods: in a first step, you use the 'connected components' method for visualising pores in space and then in a second step you characterise the porosity histograms with your MATLAB code.

I would recommend reformulating how section 3.3 is written to make it more clear that you did two things. I would go so far as to make subsections: 1) Segmented porosity for visualisation and 2) Quantifying total porosity. In this way it becomes clearer that you did both and the reason for using the integral of the pore volume histogram becomes clearer.

Response: We used Avizo software for initial processing (i.e. rescaling and filtering) of the data and thresholding. "Connected components" with limitation of the data (i.e. limiting the connected components up to 200 connected voxels) was applied only for visualization purposes. This is described in lines 105-114.

The remainder of the pore analyses (both total porosities and shape analyses) were performed by implementing Matlab scripts using the whole threshold range in numerical format (look at lines 116-117 (now in line 118) "Instead, the volumes of segmented materials (including cracks) were exported from Avizo software in numerical format"

We acknowledge the fact that the reviewer was confused about our methodology. Thus, in order to make the text easier to follow, in line 117 we added the following clarification:

"Therefore, "connected components" with limit of 200 connected voxels were used only for visualization purposes."

Of course then you would require a further subsection for the description of pore geometry (ie. the use of the covariance matrix), of which I presumed you have used pores from the 'connected components' methods but limited to the size range you stated.

Response: No, as stated in lines 116-117 ("Instead, the volumes of segmented materials (including cracks) were exported from Avizo software in numerical format") the pore sizes were not limited by the function "connected components". Any further data manipulation was performed on Matlab.

To clarify this, we changed the statement in lines 116-117 (now in line 118) to:

"Instead, the volumes and shape characteristics of segmented materials (including cracks) were exported from Avizo software in numerical format"

And also, in line 125 we replace "Pore shapes were analyzed on bivariate histograms." with "Pore shapes were analyzed on bivariate histograms plotted on Matlab by using the numerical pore characteristics, previously extracted from Avizo software."

#### Lines 123 - 130: Pore shape descriptors

The manuscript would significantly benefit from a figure illustrating the relevant aspects of the use of the covariance matrix. For example, I do not understand the author's characterisation of sphericity. I may have misunderstood the description but the ratio of two eigenvalues, which are both contained within a plane, surely cannot describe the deviation/tendency to a sphere, or have I misunderstood the metric you present? I am more familiar with sphericity being the ratio of the equivalent surface area of a sphere with the same volume as the pore volume over the actual surface area of the pore volume (e.g. Wadell, H. (1932))?

For this reason, I think that the section would benefit enormously from an example figure that corresponds to, and visualises the explanation of the metric. I imagine this would be best done with some specific examples of pore volumes from your data set. If the authors have not come up with the method themselves then I think that a citation for the more curious reader is also necessary.

Wadell, H., 1932. Volume, shape, and roundness of rock particles. *The Journal of Geology*, 40(5), pp.443-451.

Response: Thank you for this comment. No, we have not come up with the methods ourselves. All the shape analyses we performed are based on functions embedded in Avizo software that yield volumetric and shape characteristics for each segmented material in numerical format (lines 118). We simply plotted the results on bivariate histograms by using Matlab as stated in line 125.

We do not find it necessary to include in the manuscript a description of how the software produces those results as Avizo software is trusted source and every user/reader can refer to their library. However, here we provide a brief explanation of the functions we have used:

The covariance matrix is built on the basis of the moments of inertia and can be written as:

$$M = \begin{bmatrix} M_{2x} & M_{2xy} & M_{2xz} \\ M_{2xy} & M_{2y} & M_{2yz} \\ M_{2xz} & M_{2yz} & M_{2z} \end{bmatrix}$$

(matrix provided and implemented by Avizo software)

By using this matrix, the software computes the three eigenvalues by using a Singular Value decomposition. In an elongated ellipsoid the largest eigenvalue will describe the longest axis of the 3d object.

In this context, the deviation of the spherical form (i.e. anisotropy - a value extracted from Avizo software) is measured as 1 minus the ration of the smallest to largest eigenvalue. In a 3D object if the smallest and the longest axis are equal, the medium will have the same value as well, describing a spherical object and having numerical value = 0.

Lines 132 - 134: Pore density calculation

I think that it should be briefly mentioned how the density calculation was made. Was a kernel used? and if so how was the bandwidth chosen to account for number of data points? Or was it a point density calculation, if so what neighbourhood was used? I think the amount of information currently given is too sparse.

Response: We plotted the orientation of the longest eigenvalue of each pore on a lower hemisphere equal area stereographic projection. Thus, these stereonet do not represent pore density calculation but clusters of pores with preferred orientation. The data was plotted by using bivariate histogram bin counts implemented in Matlab (i.e. histcounts2), where:

```
[N,Xedges,Yedges] = histcounts2(X,Y,Xedges,Yedges)
```

The bivariate histogram results in bins with a predefined set of edges and the number of pore orientations that fall within each bin. This partitions X and Y into bins with the bin edges specified.

For contouring we used the countouring algorithm implemented in Matlab. Relevant lines from the script used are below:

```
% get histogram of resulting lats/longs and contour
[cs,cLats,cLons] = histcounts2(Lats,Lons,-95:10:95,-100:20:100);
cLats(end)=[]; cLons(end)=[];
cLats = cLats + (cLats(2)-cLats(1))/2;
cLons = cLons + (cLons(2)-cLons(1))/2;

% and plot it
COLORBAR = 0:25:225;
contourfm(cLats,cLons,cs,'LevelList',COLORBAR(2):COLORBAR(2):COLORBAR(end));
caxis([COLORBAR(1) COLORBAR(end)])
contourcbar
```

## 2. Questions/concern regarding total porosity calculations

My questions/concern is regarding the uncertainty associated with the filtering of pore data used and how this translates into the discussed differences in the magnitudes of the total porosity from different samples. Your TEM results show that very small pores exist, which you identify as fracture porosity and, by the general argument of the paper, could have resulted from coring. While these fractures shown in fig. 8d are below the XCT resolution, I am brought to wonder how many slightly larger pores exist that are actually induced fractures. For example, the fact that so many small pores identified by XCT are almost completely flat in shape (fig. 6) might reflect that many small fractures, that are not syn-kinematic, are retained in the analysis. Therefore for me a question that presents itself is; does a simple size threshold, as you have used, have an appropriate amount of filtering information to allow a discussion about a difference of 0.14% porosity? Stated more plainly, how do you know if the variation between samples is not just a function of the degree to which each lithology experienced the coring and retrieval? Alternatively, can you rule out that the variation of 0.14% may just be related to the uncertainty of the polynomial fitting used to cap the pore size for integration?

I am uncertain if it is correct to straightway interpret this difference of 0.14% as meaningful. I think that more interrogation of this result needs to appear in the discussion before it is taken forward as independent confirmation of other literature. It might be that the authors wish to use the bore hole and laboratory measurements of permeability that are mentioned in the text to quantitatively check if the difference of 0.14% in total porosity can account for these differences in permeability.

I am aware that this would require some assumptions when calculating but it would provide a base to the interpretation that a difference of 0.14% porosity between samples is meaningful. As currently presented I think that the result only convincingly shows that each calculated porosity is of the same order of magnitude.

Response: We understand the reviewer’s concern that big pores and small fractures could get easily misinterpreted/mislabeled in XCT datasets. This exactly is the prime reason why we decided against calculating total porosities in these samples by simply using ‘connected components’ and instead we fitted the data to a polynomial curve (mentioned in lines 115-123). We believe that implementing a mathematical approach is much more trustworthy than limiting the data based on the interpreter’s bias. Furthermore, our total porosity calculations (by using the polynomial fit) roughly coincide with the total porosities yield by calculating the total porosities based on connected components with up to 200 voxels. You can see these numbers on the table below:

DFDP-1B	polynomial fit	200 limit%
DFDP-1B 58_1.9 (Sam73)	0.10	0.10
DFDP-1B 69_2.48 (Sam79)	0.12	0.11
DFDP-1B 69_2.54 (Sam19)	0.10	0.09
DFDP-1B 69_2.57 (Sam69)	0.24	0.17

The reviewer also expressed concern about the fact that some of the very flat pores may represent fractures. We acknowledge the validity of this statement. However, we believe that our approach of excluding cracks is efficient and possibly the best methodology for analyzing these samples (i.e. fitting the data to a polynomial curve). Furthermore, the shape of these pores is also very likely to result from their distribution along grain boundaries, especially of clay minerals (lines 190). The authors of the manuscript are in favour of this second scenario.

And last but not least, the difference of 0.14% of total porosity in these samples may seem insignificant to the reader. However, all of the samples contain extremely low porosities, and thus only 0.14% more pores actually result in doubling the amount of pores in sample DFDP-1B 69\_2.57 in comparison to the rest of the samples. Thus, a discussion here is not only meaningful but also required, and very well related to changes in lithology in between the samples (lines 219-226, now in lines 222-229), and previous permeability measurements of these rocks (lines 233-236, now in lines 236-240).

### 3. Comment on linking XCT and TEM observations

The manuscript has a well crafted ‘red thread’ for the reader to follow but I feel that there is a gap in the current argument that requires some attention. The current formulation of the results goes from core/log scale to four very focused pictures of nano features by way of some abstract shape metrics at the micro scale. I am aware that figure 2 is supposed to bridge this gap by visualising the XCT data but it gives far too little information and doesn’t allow the reader to see that your chosen TEM images are actually representative. The reader is left trusting the authors on things that can be evidenced with your current data sets.

To address this I think that there needs to be a more tangible link between the records of the

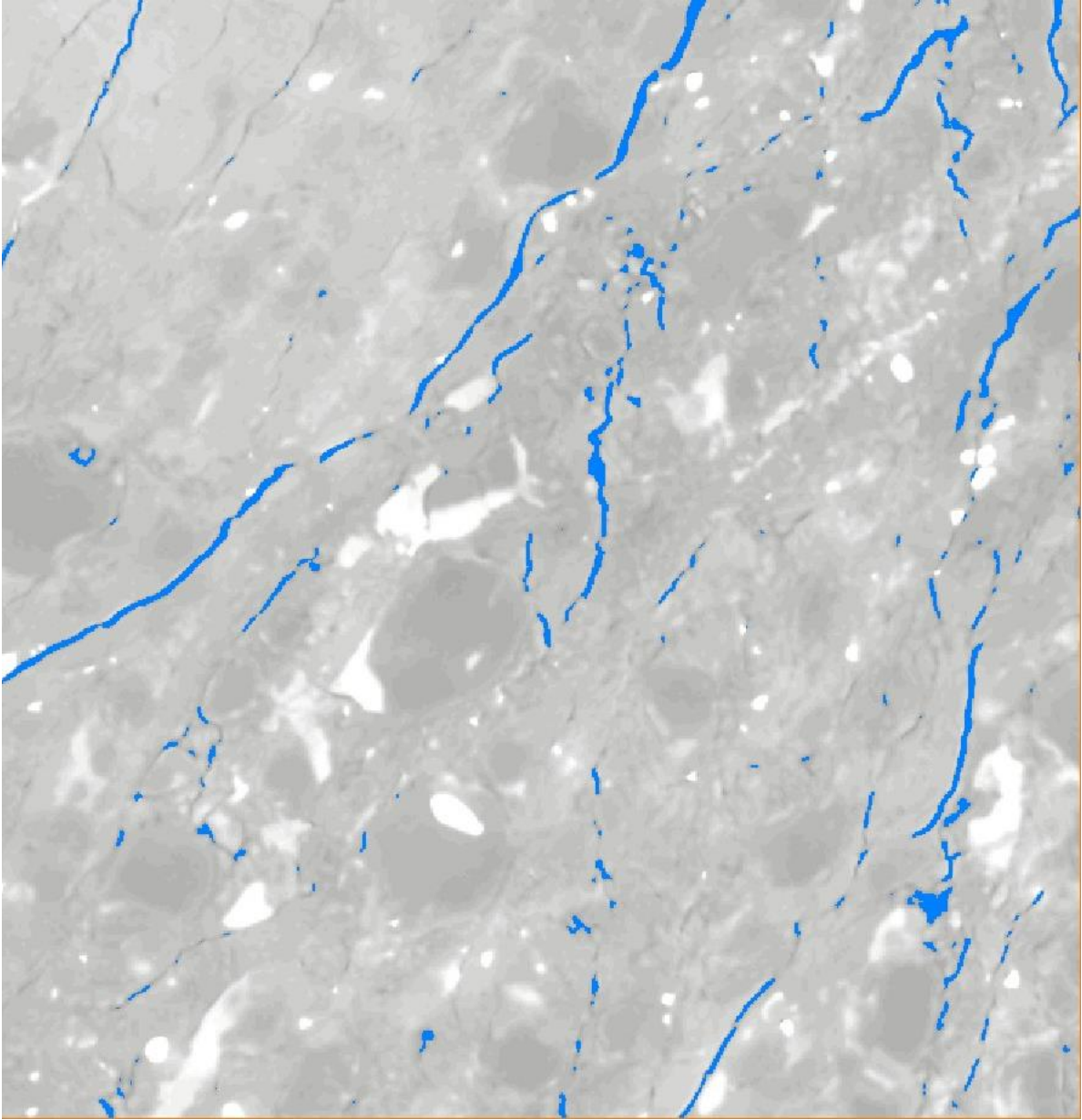
microstructure in the XCT and TEM data sets. For example, the XCT and TEM data sets should be used for comparison/corroboration of the porosity/mineral associations. The XCT data is underutilised with respect to showing the microstructure and the discussion would benefit from the evidential support that would come from the inclusion of a figure that visualises slices through the XCT data. In a very broad sense, this information showing what the microstructure looks like in the XCT data set is needed to provide a more convincing argument for the general habit of porosity (for example, that they occur 'especially' proximal to clay minerals). Currently, there are assumptions or logical jumps made by the authors in the discussion which are not necessary because the data sets at hand have information to support or falsify these suppositions. Additionally, the absence of this data was what partly led me to my comment/questions in point 2 because I was not given enough information to understand how the differences in total porosity estimates related to the different sample microstructures. Even with this aside, I would personally like to see a figure that better contextualises the micro- scale pores and their associations. Mostly I recommend this because, as I said in the general comments, your data sets are very special and as a curious reader I would like to be furnished with as much information of what the rocks look like as possible.

Response: As we mentioned in lines 184-187 (now in lines 187-190) the TEM images focus mainly on nano-scale materials, however, the largest pores observed on those images are also captured by (or comparable with) the smallest resolution of the XCT data. This justifies the validity of our argument that similar mineral – pore distribution is present both on nano- and macro-scale. This is further supported by the fact that both TEM (Fig. 8) and XCT shape analyses (Figs 4, 5 and 6) indicate the presence of predominantly elongated, flat pores (lines 188-191, now in lines 191-194 ).

Therefore, we do not agree with the reviewer's comment that there is a gap in our arguments. Instead, we think we have provided sufficient data to demonstrate to the reader the validity of our interpretation rather than asking them to trust our judgement. Furthermore, we disagree that we have underutilized our XCT datasets. Instead, most of our interpretations are based on porosity estimates, and shape analyses yield from the XCT datasets. TEM images were merely used to relate the distribution of pores in respect to different minerals and to give a microstructural context to our porosity analyses.

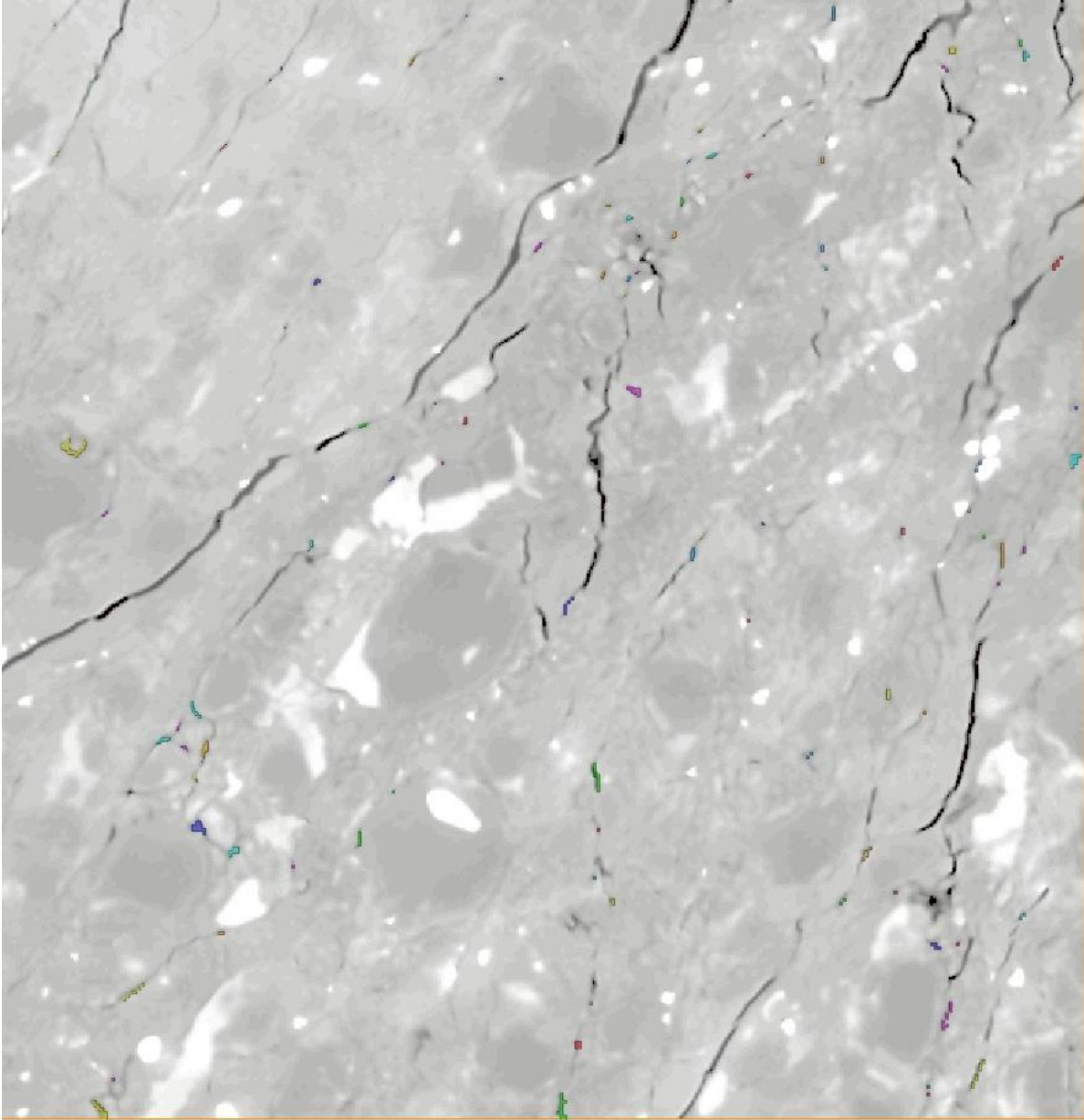
Regardless, here we show two Avizo snapshots that demonstrate that pores are distributed along grain boundaries. The examples are taken from sample DFDP-1B 69\_2.54.





Thresholded grey-greyscale image.





Grey scale image with segmented pores, marked by different colours.

#### 4. Question about section 5.3 and the concluding sentence of the manuscript

Is the porosity change not a consequence of the activity of other processes rather than a controlling factor? In the sense of your argument that the operation of mineral precipitation will lead to evaluated pore fluid pressures or fault rock weakness due to clay precipitation. Phrased as is, section 5.3 and the conclusions seem to make two arguments at the same time: the first giving the impression that porosity can provide a driving force for change and the second that its change is just a marker for the increased activity of other processes which will drive change. I would argue, within the framework of your manuscript, that changes in porosity only chart the activity of other processes that actively dissipate energy and the activity of these other processes ultimately control fault rock stability.

Response: This is a very good point, thank you. In section 5.3, we aim to demonstrate to the reader that porosity is very closely interlinked with fluid circulation and mineral precipitation, both of which may change the mechanical behaviour of the rocks, and thus trigger an earthquake. However, the amount of porosity and/or the presence of porosity in these rocks defines how these processes may evolve. Therefore, the state of porosity in these rocks plays a key role, and thus we conclude that the porosity is actually a controlling factor on the mechanical behaviour of the Alpine Fault.

#### 5. Clarification of the word overpressure

As a last comment, I would recommend that the word overpressure is defined somewhere in the introduction. It is featured prominently in the first sentence and second last sentence of the abstract as well as the manuscript's conclusions but I am not sure to what the authors mean by it. I ask because it was my understanding that the bore hole fluid pressure measurements of Sutherland et al. (2012) found that, while fluid pressure was compartmentalised around the fault, the fluid pressure was never above hydrostatic. It may be worth a sentence or two that elaborates if the authors are referring to elevated fluid pressures or fluid pressures that exceed hydrostatic or some other meaning. Alternatively, the authors may not need to use the word overpressure as I think that the word is never mentioned in the discussion.

Sutherland, R., Toy, V.G., Townend, J., Cox, S.C., Eccles, J.D., Faulkner, D.R., Prior, D.J., Norris, R.J., Mariani, E., Boulton, C. and Carpenter, B.M., 2012. Drilling reveals fluid control on architecture and rupture of the Alpine fault, New Zealand. *Geology*, 40(12), pp.1143-1146.

Response: We are familiar with the work of Sutherland et al. (2012), and we do agree with it. In addition, our work further supports the conclusions in their study (lines 237-239, now in lines 240-242). We do not state anywhere in our manuscript that fluid overpressure has been achieved in these rocks. We only speculate that the very low total porosities in these rocks and the processes affected by them (i.e. mineral precipitation and fluid circulation) can eventually lead to fluid overpressure, and thus trigger an earthquake. But in order to avoid confusion caused by different terminology, we will replace "fluid overpressure" with "elevated pore fluid pressures". (lines 17, 27, 272)

#### Technical corrections:

Line 70: '...gouge zone with predominantly random fabric...' to '...gouge zone with a predominantly random fabric...'

Response: Thank you. We will modify the text.

Line 71: 'This cohesive but uncemented layer has significantly...' to 'This cohesive but uncemented layer has a significantly...'

Response: The correction will be introduced in the text.

Line 88: 'Detailed lithological and microstructural description...' to 'Detailed lithological and microstructural descriptions...'

Response: We will modify the text accordingly.

# Interactive comment on “Micro- and nano-porosity of the active Alpine Fault zone, New Zealand” by Martina Kirilova et al.

Michel Bestmann (Referee)

michel.bestmann@fau.de

Received and published: 30 June 2020

In this research article the porosity distribution core samples of the Deep Fault Drilling project of the New Zealand Alpine Fault were investigated. Based on Synchrotron Xray microtomography (3D data set) in combination with TEM analysis (2D data set) the porosity data were interpreted with respect of the permeability, fluid mobility and the possibility of fluid overpressure and their effects on the seismic cycle. The authors were able to show that fluid overpressurization in the Alpine Fault core controlled the mechanical behaviour of the fault and could be responsible for future rupture initiation. The article is very well written and organized and provide very important data and interpretation to understand more in detail the processes, which control the seismic cycle of active fault zones. I only have minor comments on the manuscript.

General comments:

1. Portion/fraction of weak minerals related to fluid overpressure in relation to pre- existent weak minerals (clay minerals in gouge zone / fault zone) - Abstract (line 25-29) and chapter 5.3 line 245-261:

You analyses gouge material, especially clay minerals. In chapter 2. you mentioned that the gouge material is a reworked product probably as a result of ultracomminution due to multiple shear events under brittle conditions. The local presence of authigenic smectite clays (Schleicher et al., 2015) and calcite and/or chlorite mineralization within sealed fractures and in the gouge matrix (Williams et al, 2017) indicate that mineral reactions are restricted to an alteration zone within the fault core.

You conclude that due to fluid overpressure a weak mineral phase was introduced into the fault zone. My Question: What portion/fraction of the gouge material is related to the fluid overpressure and what part related to former events, e.g. ultracomminution together with fluid mobility/sealing, without fluid overpressure. Because when you already deal with a weak clay-rich rock and afterwards another weak phase in fluid- overpressurized pores is precipitated (e.g. clay, graphite), than the influence of this minor third weak phase (volume weighted with respect to the existing surrounding weak fault rock) on the already existent rheology is relatively low. Please clarify this point.

Response: Thank you for this comment. Before answering your question we would like to clarify two points: (i) the conclusion that mineral phases were introduced was documented by previous studies on these rocks (i.e. Schleicher et al., 2015 and Williams et al., 2017), our data only confirm the conclusions made in those studies; and (ii) in lines 25-29 and 245-261 (now in lines 248-264), we don't state that fluid overpressure caused the precipitation of weak mineral phases. Instead, we suggest that fluid-filled pores are favourable environment for mineral precipitation, which could further reduce the already extremely low total porosities in these rocks,

and thus lead to fluid overpressure. In this way, the addition of only small amount of new material phases could have a dramatic effect on the mechanical behaviour of the fault. Furthermore, if the newly precipitated material is with low frictional properties, the likelihood of a fault slip would be even higher.

## 2. Analytical detection of 1 $\mu\text{m}$ -sized pores

line 185-187: On figure 8b pores have sizes comparable to the small range of pores segmented on XCT images ( $> 1.3 \mu\text{m}$  in diameter), and thus we conclude that both nano- and micro pores within the Alpine Fault core are distributed on grain and phase boundaries, especially of clay minerals (Fig. 8).

MB-comment: In Fig. 8b the pores are extremely flattened /elongated and only the long g axis show a value  $> 1 \mu\text{m}$ . I am not sure if you can measure with synchrotron and a voxel size resolution of  $1.3 \mu\text{m}$  such elongates pores where the calculated diameter is  $< 1.3 \mu\text{m}$ . Please clarify this point.

Response: We do not imply we have measured the exact same pores shown on the TEM images. We only state we observe pores with comparable (but not the same) size, which allows us to suggest that the distribution of pores in these rocks is focused along grain boundaries. In response to the review by James Gilgannon, we uploaded a screenshot from Avizo that demonstrates similar distribution of pores in the micro-scale as well.

Following points are minor comments:

Line 136: High resolution TEM images

MB-comment: Actually, your TEM images are not High Resolution images. The definition of high resolution TEM imaging means that you work with an Angstrom resolution in order to make visible the atomic structure and that is not the case for your microstructures

Response: We will omit referring to the TEM images as high-resolution images. (Line 139)

line 200-201: To address this possibility more data for systematic analyses of pore orientations are needed

MB-comment: Please compare your observations/data with published papers, which contain similar TEM porosity analysis in clay-rich rocks.

Response: Our TEM observations are comparable with previous porosity studies in clay-rich rocks from the San Andreas Fault core (Janssen et al., 2011) and Nojima Fault (Surma et al., 2003) zone. Both studies document grain boundary pores, that appear with irregular and/or elongated shapes. We demonstrate such pores on Fig. 8a, b and c. In the San Andreas fault rocks pores identified as inter-clay and fracture porosity were also documented and interpreted as in-situ pores (i.e. not induced by coring or mechanical damage) whenever pores are associated with newly formed clay minerals. We show pores with similar shape characteristics and mineral associations on fig. 8b and d. However, those studies focus on pore morphology and do not discuss pore orientations.

line 229-231: Thus, the comparatively lower porosity estimates of the Alpine Fault core than other active faults (e.g. the Nojima Fault, Surma et al., 2003, and the San Andreas Fault, Blackburn et al., 2009) can be attributed to the fact that the Alpine Fault is late in its seismic cycle (Cochran et al., 2017).

MB-comment: Do you refer to the latest seismic event in the year 1717 and the average seismic cycle of  $291 \pm 23$  years? please clarify this - because maybe the reader already forgot that you have mentioned this point at the begin of the paper.

Response: Yes, we did refer to the last seismic event in 1717, and this information was provided in lines 55, 56. However, we can repeat this here to make the manuscript easier to follow. (line 234)

Figure 1 Line 403 (Figure 1):

MB-comment: Please provide GPS data of the drilling site Figure 8 (a)

Response: GPS coordinates will be added to the caption of figure 1. (line 408)

MB-comment: I presume the dark structures are the pores - please point directly with arrow-tip onto the structures. Otherwise it is a little bit confusing, especially for readers who are not familiar in reading TEM images

Response: Figures 8a and 8c are bright-field images, where porosity appears as bright contrast areas. Figures 8b and 8d are high- angle annular dark field images, where pores appear as dark contrasts areas. The arrows are positioned on the figure accordingly. However, we will add this additional information to the caption. (lines 433-434)

Figure 8 (c)

MB-comment: where are the quartz/feldspar grains with the strain shadow? Is it the grain in the middle of the image? Than please shift the text "Ellipsoidal pores" to an area in the image where it does not cover an essential part of the image.

Response: We will modify the figure.

# 1 **Micro- and nano-porosity of the active Alpine Fault zone, New** 2 **Zealand**

3 Martina Kirilova<sup>1,2</sup>, Virginia Toy<sup>1,2</sup>, Katrina Sauer<sup>1</sup>, François Renard<sup>3,4</sup>, Klaus Gessner<sup>5</sup>, Richard  
4 Wirth<sup>6</sup>, and Xianghui Xiao<sup>7,8</sup>

5 <sup>1</sup>Institut für Geowissenschaften, Johannes Gutenberg Universität Mainz, J. J. Becher Weg 21D-55128, Mainz,  
6 Germany

7  
8 ~~Department of Geology, University of Otago, PO Box 56, Dunedin 9054, New Zealand~~

9 ~~<sup>2</sup>Institut für Geowissenschaften, Johannes Gutenberg Universität Mainz, J. J. Becher Weg 21D-55128, Mainz,~~  
10 ~~Germany~~ Department of Geology, University of Otago, PO Box 56, Dunedin 9054, New Zealand

11 <sup>3</sup>Department of Geosciences, The Njord Center, University of Oslo, Oslo 0316, Norway.

12 <sup>4</sup>Université Grenoble Alpes, Université Savoie Mont Blanc, CNRS, IRD, IFSTTAR, ISTerre, BP53, 38041  
13 Grenoble, France.

14 ~~<sup>5</sup>Geological Survey of Western Australia, 100 Plain Street, East Perth, WA 6004, Australia.~~ School of Earth  
15 Sciences, The University of Western Australia, 35 Stirling Highway, Crawley, WA 6009

16 <sup>6</sup>Helmholtz-Zentrum Potsdam, GFZ, Sektion 4.3, Telegrafenberg, 14473 Potsdam, Germany

17 <sup>7</sup>Advanced Photon Source, Argonne National Laboratory, Lemont, IL 60439, USA

18 <sup>8</sup>National Synchrotron Light Source II, Brookhaven National Laboratory, Upton, NY 11973, USA

19 *Correspondence to:* Martina Kirilova ([martina.kirilova@uni-mainz.de](mailto:martina.kirilova@uni-mainz.de))

## 20 **Abstract**

21 Porosity reduction in rocks from a fault core can cause ~~fluid overpressure~~ elevated pore fluid pressures, and  
22 consequently influence the recurrence time of earthquakes. We investigated the porosity distribution in the New  
23 Zealand's Alpine Fault core in samples recovered during the first phase of the Deep Fault Drilling Project (DFDP-  
24 1B) by using two-dimensional nanoscale and three-dimensional microscale imaging. Synchrotron X-ray  
25 microtomography-derived analyses of open pore spaces show total microscale porosities in the range of 0.1 to  
26 0.24%. These pores have mainly non-spherical, elongated, flat shapes and show subtle bipolar orientation.  
27 Transmission electron microscopy reveals that nanoscale pores ornament grain boundaries of the gouge material,  
28 especially clay minerals. Our data implies that: (i) the distribution of clay minerals controls the shape and orientation  
29 of the associated pores; (ii) porosity was reduced due to pressure solution processes; and (iii) mineral precipitation in  
30 fluid-filled pores can affect the mechanical behaviour of the Alpine Fault by decreasing the already critically low  
31 total porosity of the fault core, causing elevated pore fluid pressures ~~fluid overpressure~~, and/or introducing weak  
32 mineral phases, and thus lowering the overall fault frictional strength. We conclude that the current state of porosity  
33 in the Alpine Fault core is likely to play a key role in the initiation of the next fault rupture.



## 34 **1. Introduction**

35 Fault mechanics, fault structure and fluid flow properties of damaged fault rocks are intimately related (Gratier and  
36 Gueydan, 2007; Faulkner et al., 2010). Fault rupture is associated with intense brittle fracturing that enhances  
37 porosity, and thus permeability, and therefore also possible rates and directions of fluid propagation within fault  
38 zones (Girault et al., 2018). Conversely, post seismic recovery mechanisms (gouge compaction and pressure  
39 solution processes) result in porosity, permeability and fluid flow propagation reductions (Renard et al, 2000;  
40 Faulkner et al., 2010; Sutherland et al., 2012). These processes may cause elevated pore fluid pressures within fault  
41 cores, and trigger frictional failure (Sibson, 1990; Gratier et al., 2003). Therefore, the state of porosity within rocks  
42 from fault cores can play a key role in fault slip.

43 The Alpine Fault of New Zealand is late in its seismic cycle (Cochran et al., 2017), so studying it allows us to  
44 investigate pre-earthquake conditions that may influence earthquake nucleation and rupture processes. Recently,  
45 drilling operations were undertaken in this fault zone to investigate the *in situ* conditions (Sutherland et al, 2012,  
46 2017). Slug tests in the DFDP-1B borehole (Sutherland et al., 2012) and laboratory permeability measurements of  
47 core samples (Carpenter et al., 2014) indicate permeability decreases by six orders of magnitude with increasing  
48 proximity to the fault. Furthermore, Sutherland et al. (2012) documented a 0.53 MPa fluid pressure difference across  
49 the principal slip zone (PSZ) of the fault, which suggests that the fault core has significantly lower permeability than  
50 the surrounding cataclasite units. It is therefore interpreted to act as a fault seal that limits fluid circulation within its  
51 hanging wall (Sutherland et al., 2012). Permeability variations like this are closely associated with the porosity  
52 evolution of fault cores, and thus are likely to affect the fault strength and seismic properties (Sibson, 1990; Renard  
53 et al., 2000; Gratier and Gueydan, 2007).

54 In this study, we investigate the porosity distribution in rocks from the Alpine Fault core and consider the potential  
55 effects of this porosity on fault strength. We have measured open pore spaces in these rocks from X-ray computed  
56 tomography (XCT) datasets and examined pore morphology by implementing quantitative shape analyses and using  
57 transmission electron microscopy (TEM).

## 58 **2. Geological setting**

59 New Zealand's Alpine Fault (Fig. 1a) is a major active crustal-scale structure that ruptures in a large earthquake  
60 every  $291 \pm 23$  years, the last one of which occurred in 1717 (Cochran et al., 2017). The fault is the main constituent  
61 of the oblique transform boundary between the Australian Plate and the Pacific Plate, accommodating around 75%  
62 of the relative plate motion. Ongoing dextral strike-slip at  $27 \pm 5$  mm yr<sup>-1</sup> along the fault has resulted in a total  
63 strike-separation of  $\sim 480$  km over the last 25 Ma (Norris and Cooper, 1995, 2001; Norris and Toy, 2014). In  
64 Neogene time, a dip-slip component added to the fault motion has resulted in more than 20 km of vertical uplift of  
65 the hanging wall (Norris and Cooper, 1995, 2001; Norris and Toy, 2014). Consequently, rocks comprising the  
66 hanging wall of the fault have been exposed in various outcrops, where they can be studied in detail. The  
67 amphibolite facies Alpine Schist is the metamorphic protolith of a  $\sim 1$  km thick mylonite zone, which has been  
68 exhumed from depth and now structurally overlies an up to 50 m thick zone of brittlely deformed cataclasites and

69 gouges (e.g. Norris and Cooper, 1995, 2001; Norris and Toy, 2014). These rocks have been investigated in outcrops  
70 and from samples collected in three boreholes during the two phases of the Deep Fault Drilling Project (DFDP-1A,  
71 DFDP-1B and DFDP-2B; Fig. 1a) along the Alpine Fault (Sutherland et al., 2012; Toy et al., 2015; Toy et al., 2017).

72 Most of the brittle shear displacement along the fault has been accommodated within the fault core, which includes  
73 Principal Slip Zone (PSZ) gouges and cataclasite-series rocks (Toy et al., 2015). Both in surface outcrops and drill  
74 core samples, the Alpine Fault manifests as a thin (5 to 20 cm thick) gouge zone with a predominantly random fabric  
75 of clay-rich material (Toy et al., 2015; Schuck et al., 2020). This cohesive but uncemented layer has a significantly  
76 finer grain size than the surrounding cataclasite units, which shows that the material was reworked only within this  
77 layer, most probably as a result of ultracomminution due to multiple shear events under brittle conditions (Boulton  
78 et al., 2012; Toy et al., 2015). The local presence of authigenic smectite clays (Schleicher et al., 2015) and calcite  
79 and/or chlorite mineralization within sealed fractures and in the gouge matrix (Williams et al, 2017) indicate that  
80 mineral reactions are restricted to an alteration zone within the fault core (Sutherland et al., 2012; Schuck et al.,  
81 2020). The Alpine Fault core has been interpreted to have formed during a cyclical history of mineralization, shear,  
82 and fragmentation (Toy et al., 2015). In addition, in the DFDP-1B borehole (Fig. 1b, Sutherland et al., 2012) fault  
83 gouges occur at two distinct depths: 128.1 m (PSZ-1) and 143.85 m (PSZ-2), which shows that the slip was not  
84 localized within a single gouge layer (Toy et al., 2015).

### 85 **3. Sample description and analytical methods**

#### 86 **3.1 Samples**

87 Porosity analyses were performed on four samples representing PSZ gouges and cataclasites of the Alpine Fault  
88 core, which were recovered from the DFDP-1B borehole (Fig. 1b, c; Sutherland et al., 2012). These are DFDP-1B  
89 58\_1.9, DFDP-1B 69\_2.48, DFDP-1B 69\_2.54 and DFDP-1B 69\_2.57. Sample nomenclature includes drill core run  
90 number, section number, and centimeters measured from the top of each section. These samples were recovered  
91 from drilled depth of 126.94 m, 143.82 m, 143.88 m and 143.91 m, respectively.

92 Detailed lithological and microstructural descriptions of the DFDP-1B drill core were carried out simultaneously  
93 with, and after the drilling operations by the DFDP-1 Science Team, and these data were later summarized by Toy et  
94 al. (2015). Samples DFDP-1B 58\_1.9 and DFDP-1B 69\_2.48 belong to the upper foliated cataclasite units (Fig. 1b,  
95 c; Toy et al., 2015). These were described as ultracataclasites with gouge-filled shears located above PSZ-1 and  
96 PSZ-2 respectively. Sample DFDP-1B 69\_2.54 represents the gouge layer that defines PSZ-2, whereas sample  
97 DFDP-1B 69\_2.57 is composed of brown ultracataclasites that belong to the lower cataclasite unit (Fig. 1b, c; Toy et  
98 al., 2015).

#### 99 **3.2 X-ray computed tomography (XCT)**

100 We imaged the samples using absorption tomography, where the signal intensity depends on how electron density  
101 and bulk density attenuate a monochromatic X-ray along its path through the material (e.g. Füsseis et al. 2014). We  
102 acquired the X-ray microtomography data for this study at the 2-BM beamline of the Advanced Photon Source,

103 Argonne National Laboratories USA in December 2012. The non-cylindrical samples of ~7 mm height and ~ 4 mm  
104 diameter were mounted on a rotary stage and imaged with a beam energy of 20 keV. A charge-couple device camera  
105 collected images at 0.25° rotation steps over 180°. The voxel size was 1.3 μm. We have reconstructed the datasets  
106 with a filtered back-projection parallel beam reconstruction into 32-bit gray level volumes consisting of 2083 \* 2083  
107 \* 2083 voxels using X-TRACT (Gureyev et al., 2011).

### 108 3.3 Analyses of XCT datasets

109 Data analyses and image processing were performed using the commercial software package Avizo 9.1 (Fig. 2).  
110 Initially, the datasets were rescaled to 8-bit grey scale volumes for enhanced computer performance. In addition,  
111 small volumes of interest were cropped from the whole volume before a non-local means filter was applied to  
112 reduce noise (Buades et al., 2005). On the filtered gray-scale images, porosity was identified as the darkest phase  
113 (Fig. 2a). The corresponding gray-scale values were thresholded, and the datasets were converted into binary form.  
114 However, this threshold range also captured cracks within a sample, which are likely to result from depressurization  
115 during core recovery (Fig. 2b). To omit the cracks, thresholded components with volumes larger than the volume of  
116 200 connected voxels (439.4 μm<sup>3</sup>) were excluded from the binary label images by using the morphological  
117 operation ‘connected components’ built in software Avizo 9.1. Clusters of connected components were then created  
118 to visualize 3D volumes of segmented pore spaces (Fig. 2c).

119 Unfortunately, this methodology results in either loss of larger pores or inclusion of small cracks depending on the  
120 implemented limit of connected components, and thus calculating total porosities includes significant bias.  
121 Therefore, “connected components” with limit of 200 connected voxels were used only for visualization purposes.  
122 Instead, the volumes and shape characteristics of segmented materials (including cracks) were exported from Avizo  
123 software in numerical format, and volume distributions within a sample were plotted on a logarithmic scale in  
124 Matlab (Fig. 3). Data up to a specific volume size were fit to a polynomial curve, and then the curve was  
125 extrapolated to the X intercept, which is the expected maximum pore size (Fig. 3). Total porosities were then  
126 estimated by integrating the curve, which excludes all volumes on the right side of the curve. Total porosities are  
127 presented as a percentage of the whole sample volume (Fig. 3). The implemented equations are presented in  
128 Supplementary material 1.

129 Pore shapes were analyzed on bivariate histograms plotted on Matlab by using the numerical pore characteristics,  
130 previously extracted from Avizo software. Only pore volumes between 21.97 μm<sup>3</sup> (10 voxels) and 878.8 μm<sup>3</sup> (400  
131 voxels) were included to avoid bias in the data due to insufficient voxel count and presence of cracks, respectively.  
132 For each pore, the covariance matrix of the volume was calculated, and the three eigenvalues of this covariance  
133 matrix were extracted. These three values correspond to the three main orthogonal directions in each pore (i.e. the  
134 longest, medium and shortest axes) and we use them as proxies to describe pore geometry. Thus, their amplitudes  
135 provide information on the spatial extension of the pore and its shape. The ratio between the medium and largest  
136 eigenvalues of each pore defines its elongation (Fig. 4), the ratio between the smallest to the largest – its sphericity  
137 (Fig. 5), and the ratio of the smallest to the medium – its flatness (Fig. 6).

138 The angles  $\theta$  and  $\varphi$  that describe the orientation of the longest axis of each pore with respect to the main axis of the  
139 3D scan were calculated. These angles were translated into trend and plunge and then plotted on a lower hemisphere  
140 equal area stereographic projection with a probability density contour to display the distribution of pore unit  
141 orientations (Fig. 7).

### 142 **3.4 Transmission electron microscopy (TEM)**

143 ~~High resolution~~ TEM images were collected on a FEI Tecnai G2 F20 X-Twin transmission electron microscope,  
144 located at the German Research Centre for Geosciences (GFZ), Potsdam, Germany (Fig. 8). The instrument is  
145 equipped with field-emission gun (FEG) electron source and high-angle annular dark-field (HAADF) Detector.  
146 Images were collected from samples placed on a Gatan double-tilt holder at 200kV. TEM sample preparation was  
147 performed with focused ion beam (FIB) milling at GFZ Potsdam using a HELIOS system operated at 30 kV.

## 148 **4. Results**

### 149 **4.1 XCT-derived characteristics of porosity**

150 All samples contain low total porosities, ranging from 0.1% to 0.24% (Fig. 3). However, it should be noted that the  
151 lower cataclasite sample (DFDP-1B 69\_2.57) has twice as much pore space (Fig. 3d) as any of the other samples.  
152 The characterized pore size distributions range over almost three orders of magnitude for all samples (Fig. 3).  
153 Furthermore, the expected maximum pore size volume was estimated to be largest in the PSZ-2 sample (DFDP-1B  
154 69\_2.54), reaching  $862 \mu\text{m}^3$  (Fig. 3c).

155 In all samples, shape analyses of pores with volumes between  $21.97 \mu\text{m}^3$  (10 voxels) and  $878.8 \mu\text{m}^3$  (400 voxels)  
156 demonstrate predominantly elongated (Fig. 4), non-spherical (Fig. 5) and flat pore shapes (Fig. 6). This is  
157 particularly pronounced for the smaller pore volumes. The number of elongated pores per sample is increasing in the  
158 upper foliated cataclasites (Fig. 4a and b) with increasing proximity to PSZ-2, where most elongated pores occur  
159 (Fig. 4c). Conversely, the lower cataclasite sample demonstrates proportionally fewer elongated pores within the  
160 sample (Fig. 4d). The degree of sphericity is uniform for all samples, and pores appear as mainly non-spherical (Fig.  
161 5). Few isolated spherical pores are manifested only by small pore volumes (Fig. 5). A trend of increasing the  
162 number of flat pores is observed with increasing sample depth (Fig. 6), and most flat pores are detected in the lower  
163 cataclasite (Fig. 6d).

164 The orientations of the individual pore units show two distinctive peaks with opposite vergence, defining bipolar  
165 distributions of pore orientations (Fig. 7). The observed bipolarity is subtle in samples DFDP-1B 58\_1.9 (Fig. 7a)  
166 and DFDP-1B 69\_2.48 (Fig. 7b), and more obvious in samples DFDP-1B 69\_2.54 (Fig. 7c) and DFDP-1B 69\_2.57  
167 (Fig. 7d).

## 168 **4.2 Microstructural characteristics of porosity**

169 TEM characterization of the gouge material from PSZ-2 (sample DFDP-1B 69\_2.54) reveals that the Alpine Fault  
170 gouges have composition, comprising angular quartz and/or feldspar fragments (~200 nm in size), wrapped by  
171 smaller phyllosilicates (< 100 nm long). This random fabric is ornamented by nanoscale pores (< 50 nm), distributed  
172 along all grain and phase boundaries, especially abundant along clay minerals (Fig. 8a).

173 The gouge material also demonstrates phyllosilicate-rich areas, defined by an increase in the clay/clast ratio. In these  
174 zones, fine (< 100 nm long) and coarser (few  $\mu\text{m}$  long) clay grains coexist and are aligned in wavy fabric that  
175 surrounds sporadic protolith fragments (Fig. 8b). Pore spaces are again distributed along the boundaries of the  
176 constituent mineral grains but some of them are larger (~0.5  $\mu\text{m}$ ) and ellipsoidal or elongated shape (Fig. 8b, c).  
177 These pores are commonly associated with inter-clay layer porosity. Large size pores are also observed as cracks  
178 along boundaries of quartz and/or feldspar grains (i.e. fracture porosity; Fig. 8d).

## 179 **5. Discussion**

### 180 **5.1 Characteristics of porosity within the Alpine Fault core**

181 Porosity analyses of samples from, or in close proximity to the two PSZs encountered in the DFDP-1B drill core  
182 reveal total pore volumes between ~ 0.1 and 0.24% (Fig. 3). These values are significantly lower than the porosity  
183 estimates from other active faults in the world, such as: 0.2 to 5.7% total porosity in the core of the Nojima Fault,  
184 Japan (Surma et al., 2003) and 0 to 18% in the San Andreas Fault core (Blackburn et al., 2009). The Alpine Fault  
185 core contains total pore space volumes, comparable only with the lower porosities in these previous studies. It  
186 should be noted that the smallest pore spaces captured in the XCT datasets are 1.3  $\mu\text{m}$  in size due to resolution  
187 constrains, whereas nanoscale porosity was identified on the TEM images. Therefore, the estimated total porosities  
188 represent only minimum values of the open pore spaces in the Alpine Fault core. However, the addition of nanoscale  
189 porosity volumes is unlikely to dramatically affect the final total porosity of these rocks because they comprise a  
190 very small total volume.

191 TEM images presented here mainly focus on nano-scale materials (Fig. 8a, c, d) but were also used to describe the  
192 distribution of micro-porosity in these rocks (Figure 8b). On figure 8b pores have sizes comparable to the small  
193 range of pores segmented on XCT images (> 1.3  $\mu\text{m}$  in diameter), and thus we conclude that both nano- and micro-  
194 pores within the Alpine Fault core are distributed on grain and phase boundaries, especially of clay minerals (Fig. 8).  
195 In addition, both quantitative micro-porosity shape analyses (Fig. 4, 5 and 6) and nano-pores identified on TEM  
196 images (Fig. 8) reveal that a significant population of pores are predominantly non-spherical with elongated, flat  
197 shapes. We attribute this observation to the tendency of these pores to ornament clay minerals where pores are  
198 attained and elongated along their (001) planes (Fig. 8b, c and d).

199 Foliation in the upper cataclasites is defined by clay-sized phyllosilicates, that become more abundant with  
200 proximity to the PSZ (Toy et al., 2015), where weak clay fabric is developed (Schleicher et al., 2015). This gradual  
201 enrichment in clay minerals coincides with the subtle development of bipolar distributions of pore orientations with

202 increasing sample depth (Fig. 7). This observation and the fact that pores are mainly attained along grain boundaries  
203 of clays (Fig. 8) suggest that the distribution of clay minerals also controls pore orientations within the Alpine Fault  
204 core. Previously, the phyllosilicate foliation in the Alpine Fault cataclasites has been used to define shear direction  
205 (Toy et al., 2015). Thus, we speculate that pore orientations in these rocks are also systematically related to the  
206 kinematic framework of the shear zone. If these pores represent remnants of fluid channels, their spatial orientation  
207 is likely to reflect the fluid flow directions during deformation. To address this possibility more data for systematic  
208 analyses of pore orientations are needed.

## 209 **5.2 Porosity reduction within the Alpine Fault core**

210 Porosity of the fault core is considered to evolve during the seismic cycle when fault rupture can cause porosity  
211 increase up to 10% (Marone et al., 1990), and the consequent healing mechanisms lead to porosity decrease over  
212 time due to mechanical compaction of the fault gouge and/or elimination of pore spaces within the fault core due to  
213 pressure solution processes (Sibson, 1990; Renard et al., 2000; Faulkner et al., 2010). TEM data presented here  
214 show abundance of newly precipitated authigenic clays, wrapped around coarser clay minerals (Fig. 8b).  
215 Furthermore, delicate clay minerals form fringe structures (Fig. 8a), and strain shadows (Fig. 8c) around larger  
216 quartz-feldspar grains. These microstructural observations demonstrate that pressure solution processes operated  
217 within these rocks.

218 Evidence for pressure solution processes has been previously documented in all units, comprising the Alpine Fault  
219 core (Toy et al., 2015). Abundant precipitation of alteration minerals (Sutherland et al., 2012), calcite filled  
220 intragranular and cross-cutting veins (Williams et al., 2017), and the occurrence of newly formed smectite clays  
221 (Schleicher et al., 2015) indicate extensive fluid-rock reactions. In addition, anastomosing networks of opaque  
222 minerals (such as graphite; Kirilova et al., 2017), which define foliation in the upper cataclasites (Toy et al., 2015),  
223 have been interpreted to be concentrated by pressure solution processes during aseismic creep (Toy et al., 2015;  
224 Gratier et al., 2011). The petrological characteristics of the Alpine Fault core lithologies identify solution transfer  
225 mechanisms likely were the dominant mechanism for pore closure within these rocks.

226 Post-rupture porosity reduction is known to operate three to four times faster within fine-grained fault gouges than in  
227 coarser-grained cataclasites (Walder and Nur, 1984; Sleep and Blanpied, 1992; Renard et al., 2000), which may  
228 explain the differences in total porosity between the gouge-containing samples and the footwall ultracataclasite –  
229 DFDP-1B 69-2.57 (Fig. 3). Furthermore, previous studies documented less carbonate and phyllosilicate filling of  
230 cracks in the Alpine Fault footwall cataclasites as compared to the hanging wall cataclasites (Sutherland et al., 2012;  
231 Toy et al., 2015), suggesting more reactive fluids are present and isolated within the hanging wall of the Alpine  
232 Fault. Thus, more intense dissolution-precipitation processes took place in the fault's hanging wall, which very  
233 likely resulted in more efficient porosity reduction, as demonstrated by our porosity estimates (Fig. 3).

234 As aforementioned, porosity reduction is known to increase with time after an earthquake event due to post-rupture  
235 healing mechanisms (Sibson, 1990; Renard et al., 2000; Faulkner et al., 2010). Thus, the comparatively lower  
236 porosity estimates of the Alpine Fault core than other active faults (e.g. the Nojima Fault, Surma et al., 2003, and the



237 San Andreas Fault, Blackburn et al., 2009) can be attributed to the fact that the Alpine Fault is late in its seismic  
238 cycle and the last seismic event occurred in 1717. (Cochran et al., 2017).

### 239 **5.3 Effects of porosity on the Alpine Fault strength**

240 The extremely low porosity estimates presented here (Fig. 3) are consistent with the low permeabilities of  $10^{-18}$  m<sup>2</sup>  
241 measured experimentally in clay-rich cataclasites and gouges from the Alpine Fault zone (Carpenter et al., 2014). In  
242 addition, the documented difference of total porosities between the hanging wall and footwall samples (Fig. 3)  
243 implies different intensity of pressure solution processes, and thus compartmented fluid propagation. Our data thus  
244 provide independent verification of the permeability measurements in that study (Carpenter et al., 2014) and  
245 increased confidence in their interpretation of a permeability gradient with distance from the PSZ, which itself acts  
246 as a hydraulic seal (Sutherland, et al., 2012). The existence of such a barrier to flow is characteristic for faults  
247 undergoing creep and locked faults (Rice, 1992; Labaume et al., 1997; Wiersberg and Erzinger, 2008). However,  
248 much higher permeabilities in the surrounding damaged rocks (Carpenter et al., 2014) allow fast propagation of  
249 fluids within them and can cause localization of high fluid pressures on one side or the other of a hydraulic seal  
250 (Sibson, 1990). Such fluid pressures can enhance gouge compaction and pressure solution processes within the fault  
251 core, which will eventually introduce zones of weakness and thus may trigger fault slip (Faulkner et al., 2010).

252 Previous studies and the observations presented here show that fluids were present in the Alpine Fault rocks. Fluid-  
253 filled pores represent a favorable environment for mineral precipitation, which can affect the fault strength in two  
254 ways: (i) very small decrease of these critically low total porosities due to mineral precipitation would cause fluid  
255 pressurization, a well-known fault weakening mechanism (Byerlee, 1990; Sibson, 1990); (ii) deposition of  
256 frictionally weak phases (such as clay minerals and graphite), especially if they decorate grain contacts and/or form  
257 interlinked weak layers, would lower the overall frictional strength (Rutter et al., 1976; Niemeijer et al., 2010).

258 Precipitation of authigenic clay minerals was identified on our TEM data (Fig. 8) and also documented by previous  
259 studies (Schleicher et al., 2015). As well as having low frictional strengths (Moore and Lockner, 2004), clay  
260 minerals may also contribute to the formation of an impermeable seal if they form an aligned fabric, and thus can  
261 enhance the likelihood of fluid-pressurization in the fault rocks (Rice, 1992; Faulkner et al., 2010). In addition,  
262 graphite may effectively weaken the fault due to mechanical smearing (Rutter et al., 2013) and/or localized  
263 precipitation within strained areas (Upton and Craw, 2008). Such graphite precipitation within shear surfaces was  
264 previously documented by Kirilova et al. (2017).

265 In summary, the presence of trapped fluids in the low porosity rocks of the Alpine Fault core possibly controls the  
266 mechanical behavior of the fault and could be responsible for future rupture initiation due to fluid pressurization  
267 and/or precipitation of weak mineral phases. This hypothesis is further supported by an experimental study showing  
268 that the DFDP-1 gouges are frictionally strong in the absence of elevated fluid pressure (Boulton et al., 2014).

## 269 **6. Conclusions**

270 Analyses of XCT-datasets and TEM images of borehole samples from the core of the Alpine Fault reveal micro- and  
271 nanoscale pores, distributed along grain boundaries of the constituent mineral phases, especially clay minerals. The  
272 tendency of these pores to ornament clays defines their predominantly non-spherical, elongated, flat shapes and the  
273 bipolar distribution of pore orientations. The documented extremely low total porosities (from 0.1 to 0.24 %) in  
274 these rocks suggest effective porosity reduction. Microstructural observations presented here and documented in  
275 previous studies indicate that pressure solution processes were the dominant healing mechanism, and that fluids  
276 were present in these rocks. Therefore, fluid-filled pores may be places where ~~fluid overpressures~~ elevated pore fluid  
277 pressures develop, due to further mineral precipitation that decreases the already critically low total porosities.  
278 Alternatively, they may also facilitate deposition of weak mineral phases (such as clay minerals and graphite) that  
279 may very effectively weaken the fault. We conclude that the current state of the fault core porosity is possibly a  
280 controlling factor on the mechanical behaviour of the Alpine Fault and will likely play a key role in the initiation of  
281 the next fault rupture.

### 282 **Data availability.**

283 Matlab code and numerical data of pore volumes can be found in Supplementary material 1.

### 284 **Authors contribution**

285 Kirilova reconstructed, processed, and analysed the XCT datasets presented here, interpreted the TEM data and  
286 prepared the manuscript. Most of this work was performed during Kirilova's PhD under the academic guidance of  
287 Toy. Toy and Gessner collected the XCT data with technical support by Xiao. Renard and Sauer contributed with  
288 valuable discussion about XCT data analyses. Wirth enabled TEM data acquisition and provided his expertise on  
289 TEM data interpretation. The final version of this manuscript benefits from collective intellectual input.

### 290 **Competing interests**

291 The authors declare that they have no conflict of interest.

### 292 **Acknowledgments**

293 We gratefully acknowledge funding from the Advances Photon Source (GUP 31177). This research used resources  
294 of the Advanced Photon Source, a U.S. Department of Energy (DOE) Office of Science User Facility operated for  
295 the DOE Office of Science by Argonne National Laboratory under Contract No. DE-AC02-06CH11357. Avizo  
296 workstation was built at the University of Otago with financial support provided by Nvidia, Corporation Royal  
297 Society of New Zealand's Rutherford fellowships (16-UOO-001), the Ministry of Business and Innovation's  
298 Endeavor Fund (C05X1605/GNS-MBIE00056), and a subcontract to the Tectonics and Structure of Zealandia  
299 Program at GNS Science (GNS-DCF00020). Publishing bursary funding provided by the University of Otago is  
300 greatly appreciated. We thank Sherry Mayo for helping with the reconstruction process of XCT data and Andrew  
301 Squelch for providing use of the Avizo workstation, located at CSIRO, Perth, Australia during the initial data

302 analyses. Special thanks to Reed Debaets for assistance with the development of Matlab code. [Klaus Gessner](#)  
303 [publishes with permission of the Executive Director, Geological Survey of Western Australia.](#)

## 304 **References**

305 Berryman, K. R., Cochran, U. A., Clark, K. J., Biasi, G. P., Langridge, R. M., and Villamor, P., 2012, Major  
306 earthquakes occur regularly on an isolated plate boundary fault, *Science*, 336(6089), 1690-1693.

307 Blackburn, E. D., Hadizadeh, J., and Babaie, H. A., 2009, A microstructural study of SAFOD gouge from actively  
308 creeping San Andreas Fault zone: Implications for shear localization models, *in* AGU Fall Meeting Abstracts.

309 Buades, A., Coll, B. and Morel, J. M., 2005, A non-local algorithm for image denoising, *in* Computer Vision and  
310 Pattern Recognition, IEEE Computer Society Conference, Vol. 2, pp. 60-65.

311 Boulton, C., Carpenter, B. M., Toy, V., and Marone, C., 2012, Physical properties of surface outcrop cataclastic  
312 fault rocks, Alpine Fault, New Zealand, *Geochemistry, Geophysics, Geosystems*, 13, Q01018,  
313 doi:10.1029/2011GC003872.

314 Boulton, C., Moore, D. E., Lockner, D. A., Toy, V. G., Townend, J., and Sutherland, R., 2014, Frictional properties  
315 of exhumed fault gouges in DFDP-1 cores, Alpine Fault, New Zealand, *Geophysical Research Letters*, 41(2), 356-  
316 362.

317 Byerlee, J., 1990, Friction, overpressure and fault normal compression, *Geophysical Research Letters*, 17(12), 2109-  
318 2112.

319 Carpenter, B. M., Kitajima, H., Sutherland, R., Townend, J., Toy, V. G., and Saffer, D. M., 2014, Hydraulic and  
320 acoustic properties of the active Alpine Fault, New Zealand: Laboratory measurements on DFDP-1 drill core, *Earth*  
321 *and Planetary Science Letters*, 390, 45-51.

322 Cochran, U. A., Clark, K. J., Howarth, J. D., Biasi, G. P., Langridge, R. M., Villamor, P., ... and Vandergoes, M. J.,  
323 2017, A plate boundary earthquake record from a wetland adjacent to the Alpine fault in New Zealand refines  
324 hazard estimates, *Earth and Planetary Science Letters*, 464, 175-188.

325 Faulkner, D. R., Jackson, C. A. L., Lunn, R. J., Schlische, R. W., Shipton, Z. K., Wibberley, C. A. J., and Withjack,  
326 M. O., 2010, A review of recent developments concerning the structure, mechanics and fluid flow properties of fault  
327 zones, *Journal of Structural Geology*, 32(11), 1557-1575.

328 Fousseis, F., Xiao, X., Schrank, C., and De Carlo, F., 2014, A brief guide to synchrotron radiation-based  
329 microtomography in (structural) geology and rock mechanics, *Journal of Structural Geology*, 65, 1-16.

330 Girault, F., Adhikari, L. B., France-Lanord, C., Agrinier, P., Koirala, B. P., Bhattarai, M., and Perrier, F., 2018,  
331 Persistent CO<sub>2</sub> emissions and hydrothermal unrest following the 2015 earthquake in Nepal, *Nature*  
332 *Communications*, 9(1), 2956.

333 Gratier, J.-P., Favreau, P., and Renard, F., 2003, Modelling fluid transfer along California faults when integrating  
334 pressure solution crack sealing and compaction processes, *Journal of Geophysical Research*, 108, 2104,  
335 doi:10.1029/2001JB000380, B2.

336 Gratier, J. P., 2011, Fault permeability and strength evolution related to fracturing and healing episodic processes  
337 (years to millennia): the role of pressure solution, *Oil and Gas Science and Technology–Revue d'IFP Energies*  
338 *nouvelles*, 66(3), 491-506.

339 Gratier, J. P., and Gueydan, F., 2007, Effect of Fracturing and Fluid–Rock Interaction on Seismic Cycles, *Tectonic*  
340 *Faults: Agents of Change on a Dynamic Earth*, 95, 319e356.

341 Gureyev, TE, Nesterets, Y, Ternovski, D, Wilkins, SW, Stevenson, AW, Sakellariou, A and Taylor, JA 2011,  
342 Toolbox for advanced x-ray image processing, in *Advances in Computational Methods for X-Ray Optics II* edited  
343 by M Sanchez del Rio and O Chubar, *Advances in Computational Methods for X-Ray Optics II*, San Diego, USA,  
344 21-25 August 2011: SPIE - The International Society of Optics and Photonics 8141.

345 Janssen, C., Wirth, R., Reinicke, A., Rybacki, E., Naumann, R., Wenk, H. R., and Dresen, G., 2011, Nanoscale  
346 porosity in SAFOD core samples (San Andreas Fault), *Earth and Planetary Science Letters*, 301(1), 179-189.

347 Labaume, P., Maltman, A. J., Bolton, A., Tessier, D., Ogawa, Y., and Takizawa, S. 1997, Scaly fabrics in sheared  
348 clays from the décollement zone of the Barbados accretionary prism, *in* Shipley, T.H., Ogawa, Y., Blum, P., and  
349 Bahr, J.M. (Eds.), *Proceedings of the Ocean Drilling Program Scientific Results*, 59-78.

350 Kirilova, M., Toy, V. G., Timms, N., Halfpenny, A., Menzies, C., Craw, D., ... and Carpenter, B. M., 2017, Textural  
351 changes of graphitic carbon by tectonic and hydrothermal processes in an active plate boundary fault zone, *Alpine*  
352 *Fault, New Zealand*, Geological Society, London, Special Publications, 453, SP453-13.

353 Marone, C., Raleigh, C. B., and Scholz, C. H., 1990, Frictional behavior and constitutive modeling of simulated  
354 fault gouge, *Journal of Geophysical Research: Solid Earth*, 95(B5), 7007-7025.

355 Niemeijer, A., Marone, C., and Elsworth, D., 2010, Fabric induced weakness of tectonic faults, *Geophysical*  
356 *Research Letters*, 37, L03304, doi:10.1029/2009GL041689.

357 Norris, R. J., and Cooper, A. F., 1995, Origin of small-scale segmentation and transpressional thrusting along the  
358 Alpine fault, New Zealand. *Geological Society of America Bulletin*, 107(2), 231-240.

359 Norris, R. J., and Cooper, A. F., 2001, Late Quaternary slip rates and slip partitioning on the Alpine Fault, New  
360 Zealand. *Journal of Structural Geology*, 23(2), 507-520.

361 Norris, R. J., and Toy, V. G., 2014, Continental transforms: A view from the Alpine Fault, *Journal of Structural*  
362 *Geology*, 64, 3-31.

363 Renard, F., Gratier, J. P., and Jamtveit, B., 2000, Kinetics of crack-sealing, intergranular pressure solution, and  
364 compaction around active faults, *Journal of Structural Geology*, 22(10), 1395-1407.

365 Rice, J. R., 1992, Fault stress states, pore pressure distributions, and the weakness of the San Andreas fault,  
366 *International Geophysics*, 51, 475-503.

367 Rutter, E. H., and Elliott, D., 1976, The kinetics of rock deformation by pressure solution, *Philosophical*  
368 *Transactions for the Royal Society of London, Series A, Mathematical and Physical Sciences*, 283, 203-219.

369 Rutter, E. H., Hackston, A. J., Yeatman, E., Brodie, K. H., Mecklenburgh, J., and May, S. E., 2013, Reduction of  
370 friction on geological faults by weak-phase smearing, *Journal of Structural Geology*, 51, 52-60.

371 Schleicher, A. M., Sutherland, R., Townend, J., Toy, V. G., and Van Der Pluijm, B. A., 2015, Clay mineral  
372 formation and fabric development in the DFDP-1B borehole, central Alpine Fault, New Zealand, *New Zealand*  
373 *Journal of Geology and Geophysics*, 58(1), 13-21.

374 Schuck, B., Schleicher, A. M., Janssen, C., Toy, V. G., and Dresen, G., 2020, Fault zone architecture of a large  
375 plate-bounding strike-slip fault: a case study from the Alpine Fault, New Zealand. *Solid Earth*, 11(1), 95-124.

376 Secor, D. T., 1965, Role of fluid pressure in jointing, *American Journal of Science*, 263(8), 633-646.

377 Sibson, R. H., 1990, Conditions for fault-valve behaviour, *Geological Society, London, Special Publications*, 54(1),  
378 15-28.

379 Sleep, N. H., and Blanpied, M. L., 1992, Creep, compaction and the weak rheology of major faults, *Nature*,  
380 359(6397), 687-692.

381 Surma, F., Géraud, Y., and Pezard, P., 2003, Porosity network of the Nojima fault zone in the Hirabayashi hole  
382 (Japan), *in* EGS-AGU-EUG Joint Assembly.

383 Sutherland, R., Eberhart-Phillips, D., Harris, R. A., Stern, T., Beavan, J., Ellis, S Henrys, S., Cox, S., Norris, R.J.,  
384 Berryman, K.R. and Townend, J., 2007, Do great earthquakes occur on the Alpine fault in central South Island, New  
385 Zealand?, In: *A continental plate boundary: tectonics at South Island, New Zealand, Geophysical Monograph,*  
386 *American Geophysical Union*, 235-251.

387 Sutherland, R., Toy, V. G., Townend, J., Cox, S. C., Eccles, J. D., Faulkner, D. R Prior, D.J., Norris, R.J., Mariani,  
388 E., Boulton, C. and Carpenter, B.M., 2012, Drilling reveals fluid control on architecture and rupture of the Alpine  
389 fault, New Zealand, *Geology*, 40(12), 1143-1146.

390 Sutherland, R., Townend, J., Toy, V., Upton, P., Coussens, J., Allen, M., and Boles, A., 2017, Extreme  
391 hydrothermal conditions at an active plate-bounding fault, *Nature*, 546, 137-140, doi: 10.1038/nature22355.

392 Toy, V. G., Boulton, C. J., Sutherland, R., Townend, J., Norris, R. J., Little, T. A., and Scott, H., 2015, Fault rock  
393 lithologies and architecture of the central Alpine fault, New Zealand, revealed by DFDP-1 drilling, *Lithosphere*,  
394 L395-1.

395 Toy, V. G., Sutherland, R., Townend, J., Allen, M., Becroft, L., Boles, A., Boulton., C., Carpenter, B., Cooper, A.,  
396 Cox, S., Daube, C., Faulkner., D., Halfpenny, A., Kato, N., Keys, S., Kirilova, M., Kometani, Y., Little, T., Mariani,  
397 E., Melosh, B., Menzies, C., Morales, L., Morgan, C., Mori, C., Niemeijer, A., ... and Zimmer, M., 2017, Bedrock  
398 Geology of DFDP-2B, Central Alpine Fault, New Zealand, *New Zealand Journal of Geology and Geophysics.*,  
399 60(4), 497-518.

400 Upton P. and Craw D., 2008, Modelling the role of graphite in development of a mineralised mid-crustal shear zone,  
401 Macraes mine, New Zealand, *Earth and Planetary Science Letters* 266: 245-255.

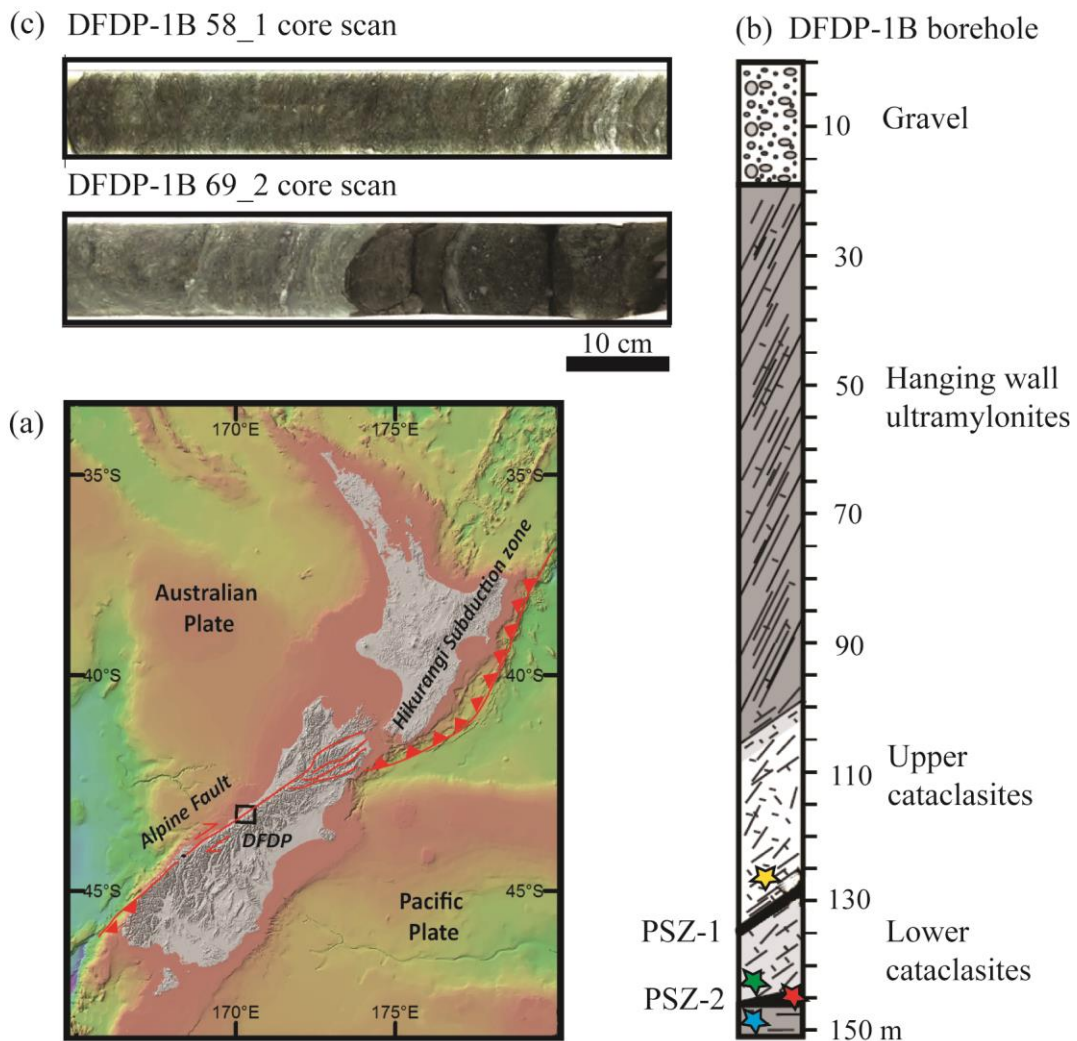
402 Walder, J., and Nur, A., 1984, Porosity reduction and crustal pore pressure development, *Journal of Geophysical*  
403 *Research: Solid Earth*, 89(B13), 11539-11548.

404 Walsh, J. B., 1965, The effect of cracks on the uniaxial elastic compression of rocks, *Journal of Geophysical*  
405 *Research*, 70(2), 399-411.

406 Wiersberg, T and Erzinger, J 2008, Origin and spatial distribution of gas at seismogenic depths of the San Andreas  
407 Fault from drill-mud gas analysis: *Applied Geochemistry*, v. 23, no. 6, p. 1675-1690.

408 Williams, J. N., Toy, V. G., Smith, S. A and Boulton, C., 2017, Fracturing, fluid-rock interaction and mineralisation  
409 during the seismic cycle along the Alpine Fault, *Journal of Structural Geology*, 103, 151-166.

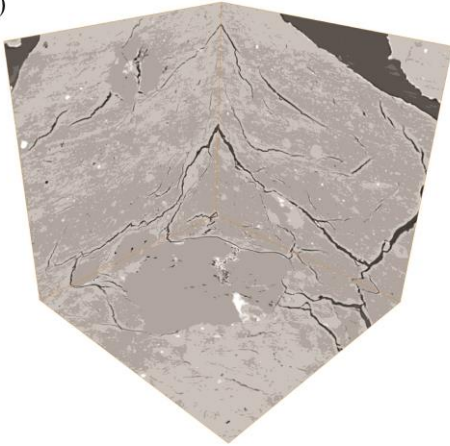




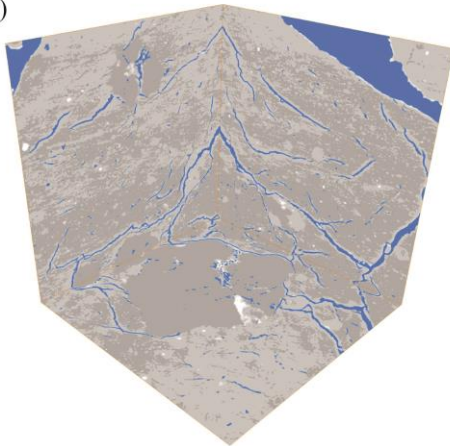
411  
 412 **Figure 1.** (a) Location map of DFDP drill sites (a bathymetric map compiled by NIWA). Drill site coordinates:  
 413 43°17'5"S, 170°24'22"E (b) Schematic diagram of the sampled lithologies in DFDP-1B borehole (modified after  
 414 Sutherland et al., 2012). (c) Scans of DFDP-1B drill core. Samples were collected from the locations indicated with  
 415 stars: yellow – DFDP-1B 58\_1.9; green – DFDP-1B 69\_2.48; red – DFDP-1B 69\_2.54; blue – DFDP-1B 69\_2.57.

DFDP - 1B 69-2.57

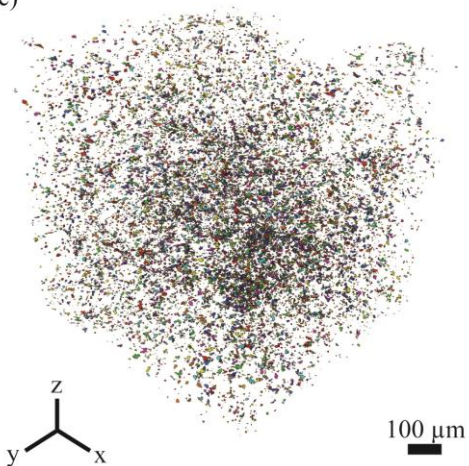
(a)



(b)



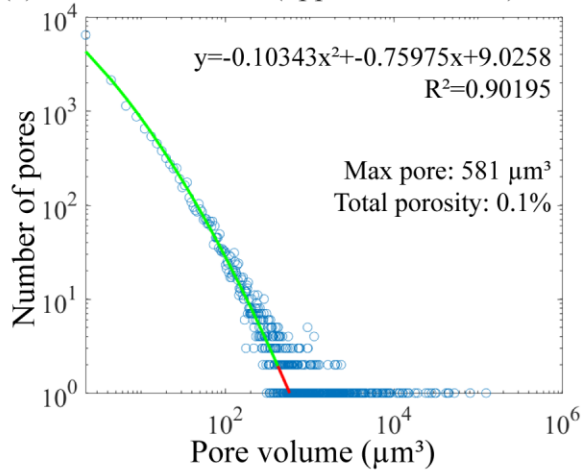
(c)



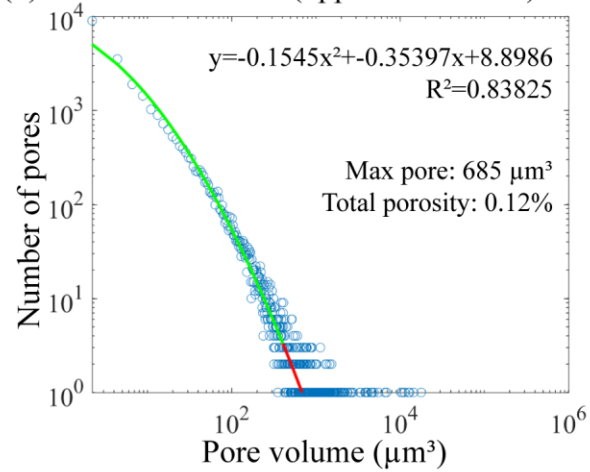
416

417 **Figure 2.** X-ray tomography data processing workflow. (a) Gray scale images in xy, xz and yz directions (b)  
418 Threshold of the darkest gray scale phase in each sample, corresponding to voids (pores and fractures); (c) 3D  
419 volume of the segmented pore spaces after the fractures due to sample decompaction and coring damaging effects  
420 were removed.

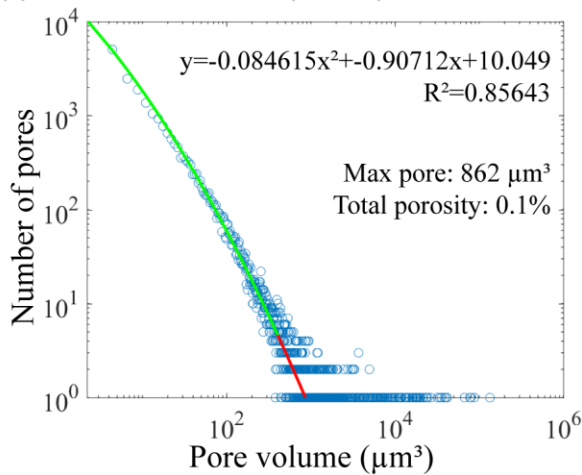
(a) DFDP-1B 58-1.9 (upper foliated ccl)



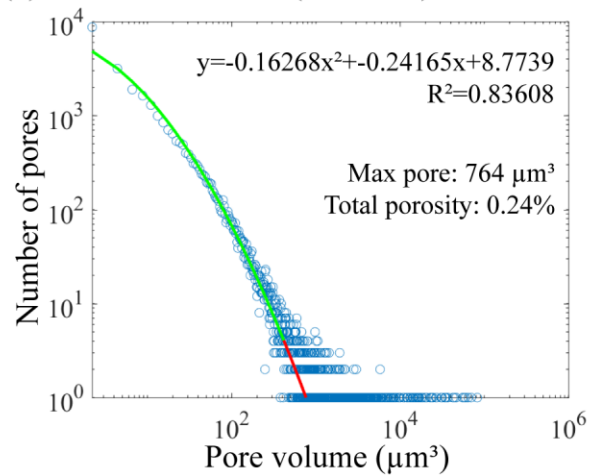
(b) DFDP-1B 69-2.48 (upper foliated ccl)



(c) DFDP-1B 69-2.54 (PSZ-2)



(d) DFDP-1B 69-2.57 (lower ccl)



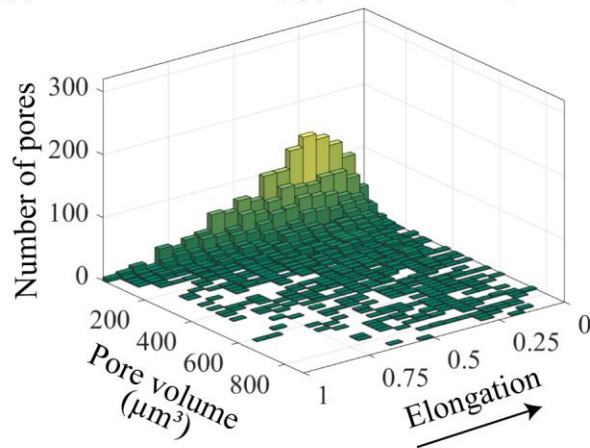
421

422

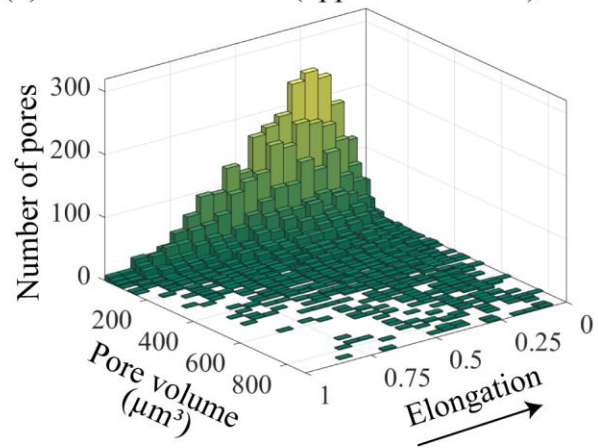
423

**Figure 3.** Plots of pore volume versus number of pores for each sample. Estimates of total porosity and size of the maximum expected pore are also shown, as well as the curve fitting function for each dataset.

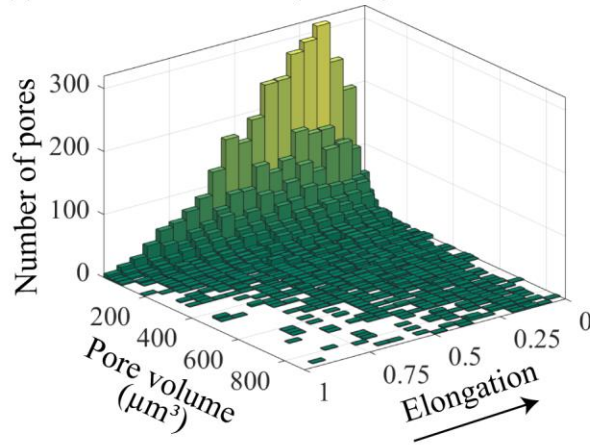
(a) DFDP-1B 58-1.9 (upper foliated ccl)



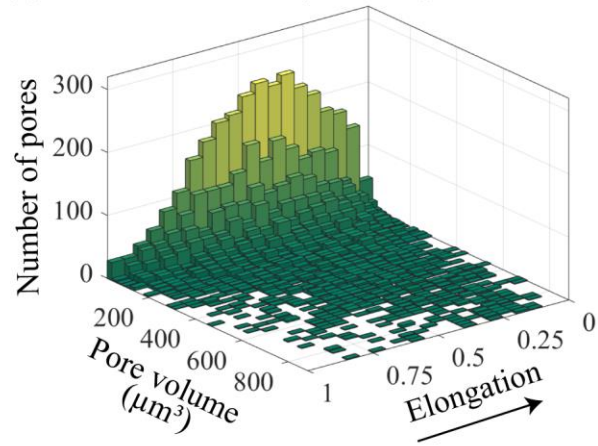
(b) DFDP-1B 69-2.48 (upper foliated ccl)



(c) DFDP-1B 69-2.54 (PSZ-2)



(d) DFDP-1B 69-2.57 (lower ccl)

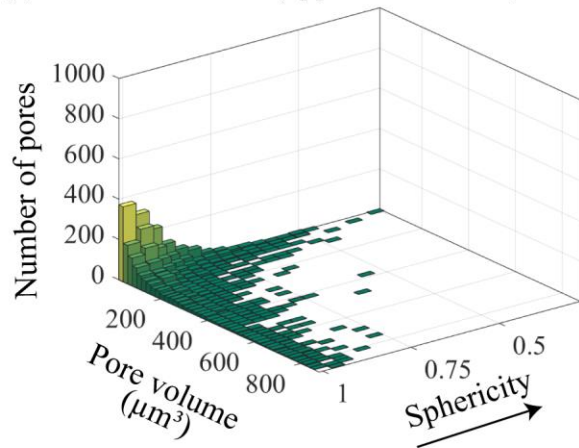


424

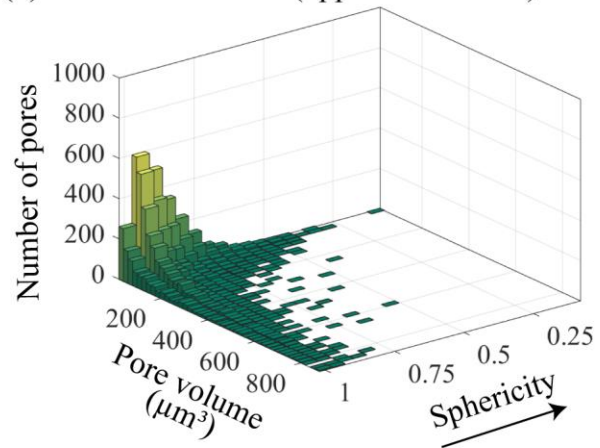
425 **Figure 4.** Bivariate histograms showing elongation versus pore volume ( $\mu\text{m}^3$ ) and number of pores for each sample.

426 The arrow indicates the direction of increasing elongation.

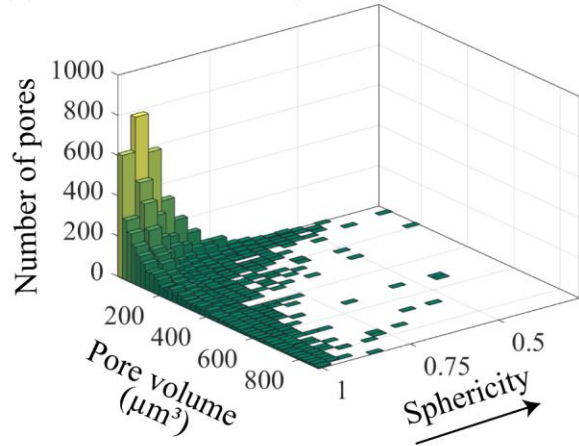
(a) DFDP-1B 58-1.9 (upper foliated ccl)



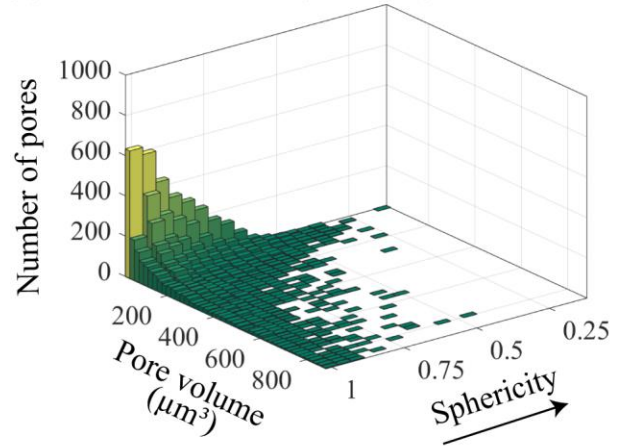
(b) DFDP-1B 69-2.48 (upper foliated ccl)



(c) DFDP-1B 69-2.54 (PSZ-2)



(d) DFDP-1B 69-2.57 (lower ccl)



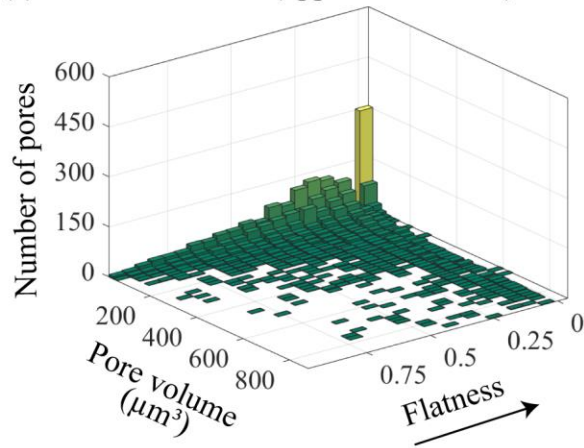
427

428 **Figure 5.** Bivariate histograms showing sphericity versus pore volume ( $\mu\text{m}^3$ ) and number of pores for each sample.

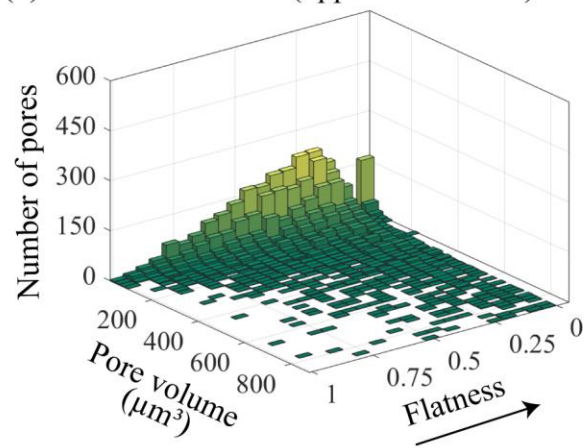
429 The arrow indicates the direction of increasing sphericity.



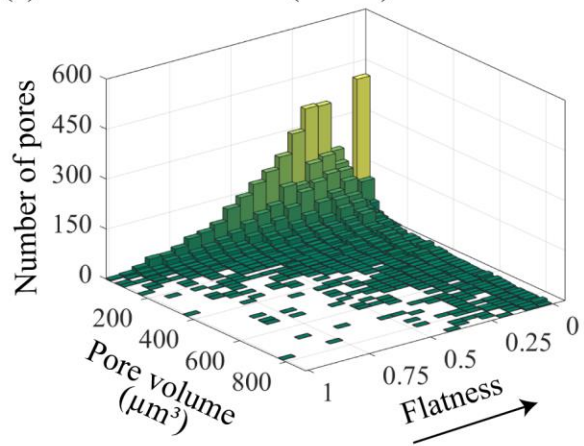
(a) DFDP-1B 58-1.9 (upper foliated ccl)



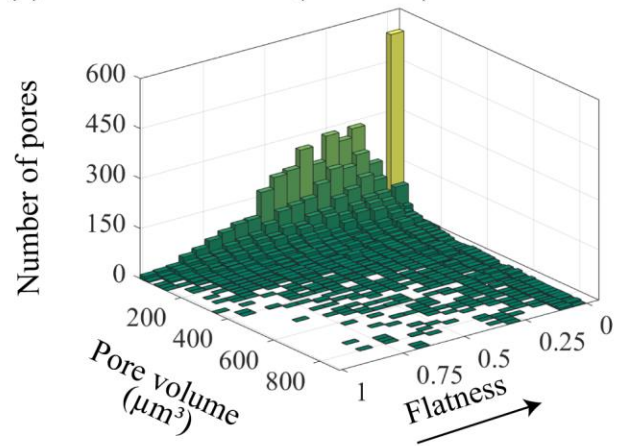
(b) DFDP-1B 69-2.48 (upper foliated ccl)



(c) DFDP-1B 69-2.54 (PSZ-2)



(d) DFDP-1B 69-2.57 (lower ccl)



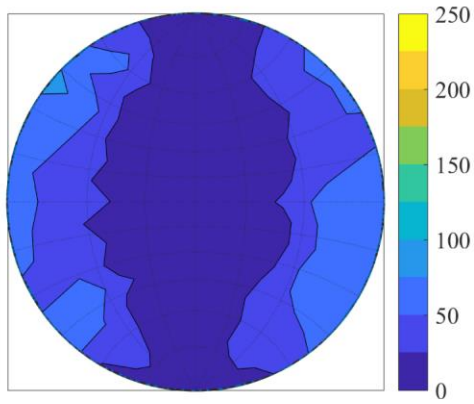
430

431 **Figure 6.** Bivariate histograms showing flatness versus pore volume ( $\mu\text{m}^3$ ) and number of pores for each sample.

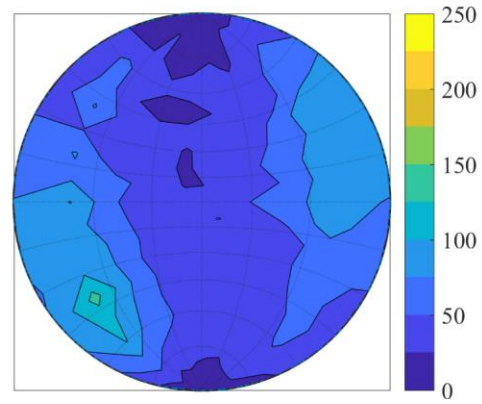
432 The arrow indicates the direction of increasing flatness.



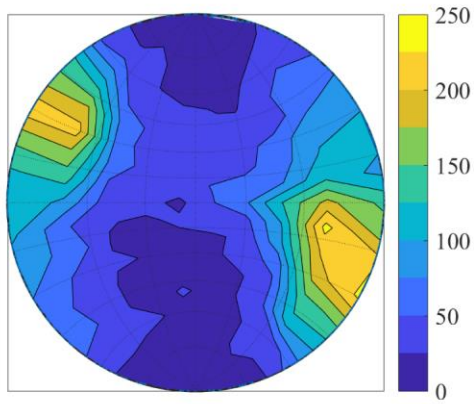
(a) DFDP-1B 58-1.9 (upper foliated ccl)



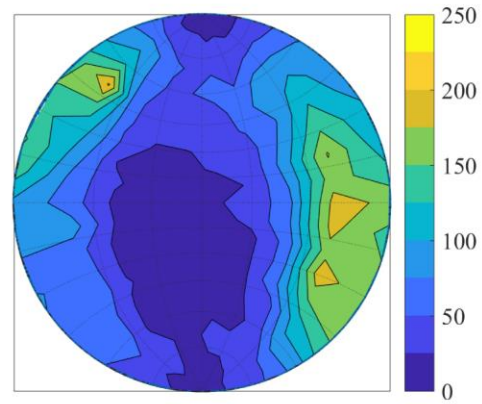
(b) DFDP-1B 69-2.48 (upper foliated ccl)



(c) DFDP-1B 69-2.54 (PSZ-2)



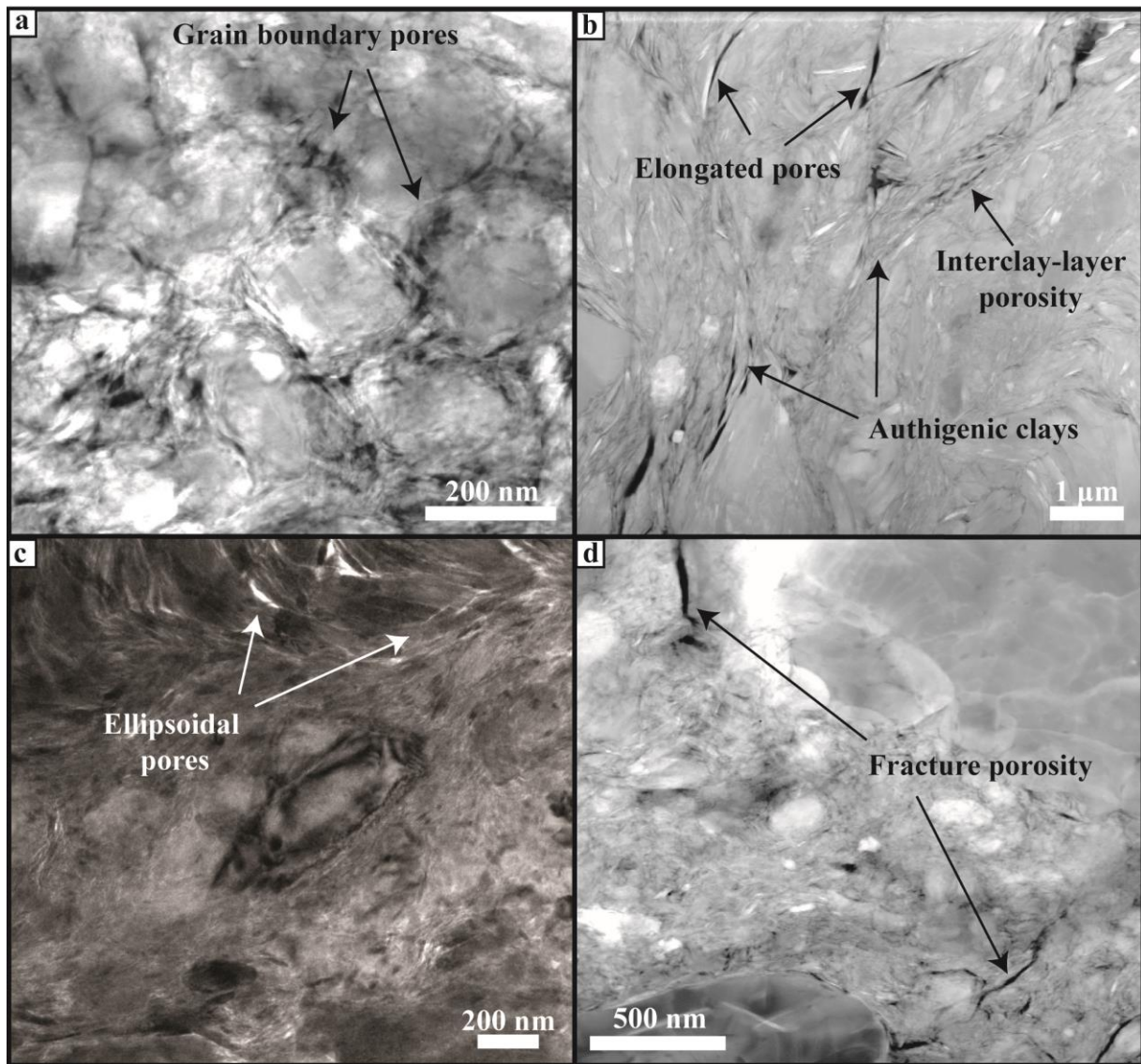
(d) DFDP-1B 69-2.57 (lower ccl)



433

434 **Figure 7.** Distribution of pore unit orientations plotted on a lower hemisphere equal area stereographic projection

435 with a probability density contour.



436  
 437 **Figure 8.** Transmission electron microscopy images collected from the gouge sample DFDP-1B 69\_2.54 (PSZ-2).  
 438 (a) and (c) are bright-field images, where porosity appears as bright contrast areas. (b) and (d) are high-angle annular  
 439 dark field images, where pores appear as dark contrasts areas. (a) TEM bright-field image of homogeneous fault  
 440 gouge area. Quartz/feldspar grains, wrapped by fine authigenic clays, displaying fringe structures. Pores with sub-  
 441 angular shape distributed along grain boundaries. (b) HAADF image of phyllosilicate-rich gouge area. Co-existence  
 442 of fine authigenic clays with coarser clay mineral grains. Elongated pores and interlayer porosity. (c) TEM bright-  
 443 filed image of ellipsoidal pores in phyllosilicate-rich areas. Examples of strain shadows along quartz/feldspar grains.  
 444 (d) HAADF image of fracture porosity along grain boundaries of quartz/feldspar grains.